New relativistic effective interaction for finite nuclei, infinite nuclear matter, and neutron stars

Bharat Kumar,[1,2] S. K. Patra,[1,2] and B. K. Agrawal[2,3]
[1]*Institute of Physics, Bhubaneswar 751005, India*
[2]*Homi Bhabha National Institute, Training School Complex, Anushakti Nagar, Mumbai 400085, India*
[3]*Saha Institute of Nuclear Physics, 1/AF, Bidhannagar, Kolkata 700064, India*

(Received 4 December 2017; revised manuscript received 7 February 2018; published 23 April 2018)

We carry out the study of finite nuclei, infinite nuclear matter, and neutron star properties with the newly developed relativistic force, the Institute of Physics Bhubaneswar-I (IOPB-I). Using this force, we calculate the binding energies, charge radii, and neutron-skin thickness for some selected nuclei. From the ground-state properties of superheavy nuclei ($Z = 120$), it is noticed that considerable shell gaps appear at neutron numbers $N = 172$, 184, and 198, manifesting the magicity at these numbers. The low-density behavior of the equation of state for pure neutron matter is compatible with other microscopic models. Along with the nuclear symmetry energy, its slope and curvature parameters at the saturation density are consistent with those extracted from various experimental data. We calculate the neutron star properties with the equation of state composed of nucleons and leptons in β-equilibrium, which are in good agreement with the x-ray observations by Steiner [Astrophys. J. **722**, 33 (2010)] and Nättilä [Astron. Astrophys. **591**, A25 (2016)]. Based on the recent observation of GW170817 with a quasi-universal relation, Rezzolla *et al.* [Astrophys. J. Lett. **852**, L25 (2018)] have set a limit for the maximum mass that can be supported against gravity by a nonrotating neutron star in the range $2.01 \pm 0.04 \lesssim M(M_\odot) \lesssim 2.16 \pm 0.03$. We find that the maximum mass of the neutron star for the IOPB-I parametrization is $2.15 M_\odot$. The radius and tidal deformability of a canonical neutron star of mass $1.4 M_\odot$ are 13.2 km and 3.9×10^{36} g cm^2 s^2, respectively.

DOI: 10.1103/PhysRevC.97.045806

I. INTRODUCTION

At present, nuclear physics and nuclear astrophysics are well described within the self-consistent effective mean-field models [1]. These effective theories are not only successful to describe the properties of finite nuclei but also explain the nuclear matter at supranormal densities [2]. Recently, a large number of nuclear phenomena were predicted near the nuclear drip lines within the relativistic and nonrelativistic formalisms [3–5]. Consequently, several experiments are planned in various laboratories to probe the deeper side of the unknown nuclear territories, i.e., the neutron and proton drip lines. Among the effective theories, the relativistic mean-field (RMF) model is one of the most successful self-consistent formalisms that is currently drawning attention to the theoretical studies of such systems.

Although the construction of the energy density functional for the RMF model is different than those for the nonrelativistic models, such as Skyrme [6,7] and Gogny interactions [8], the obtained results for finite nuclei are in general very close to each other. The same accuracy in prediction is also valid for the properties of the neutron stars. At higher densities, the relativistic effects are accounted for appropriately within the RMF model [9]. In the RMF model the interactions among nucleons are described through the exchange of mesons. These mesons are collectively taken as effective fields and denoted by classical numbers, which are the quantum mechanical expectation values. In brief, the RMF formalism is the relativistic Hartree or Hartree-Fock approximation to the one-boson exchange (OBE) theory of nuclear interactions. In OBE theory, the nucleons interact with each other by exchange of isovector π, ρ, and δ mesons and isoscalars like η, ρ, and ω mesons. The π and η mesons are pseudo-scalar in nature and do not obey the ground-state parity symmetry. At the mean-field level, they do not contribute to the ground-state properties of even nuclei.

The first and simplest successful relativistic Lagrangian is formed by taking only the contribution of the σ, ω and ρ mesons into account without any nonlinear term for the Lagrangian density. This model predicts an unreasonably large incompressibility K of $\sim$550 MeV for the infinite nuclear matter at saturation [9]. To lower the value of K to an acceptable range, the self-coupling terms in the σ meson are included by Boguta and Bodmer [10]. Based on this Lagrangian density, a large number of parameter sets, such as NL1 [11], NL2 [11], NL-SH [12], NL3 [13], and NL3* [14] were calibrated. The addition of σ-meson self-couplings improved the quality of finite nuclei properties and incompressibility remarkably. However, the equations of state at supranormal densities were quite stiff. Thus, the addition of vector meson self-coupling is introduced into the Lagrangian density and different parameter sets are constructed [15–17]. These parameter sets are able to explain the finite nuclei and nuclear matter properties to a great extent, but the existence of the Coester band as well as the three-body effects need to be addressed. Subsequently, nuclear physicists also changed their way of thinking and introduced different strategies to improve the result by designing the density-dependent coupling constants and effective-field-theory-motivated relativistic mean-field (E-RMF) model [1,18].

Further, motivated by the effective field theory, Furnstahl *et al.* [1] used all possible couplings up to fourth order of the

expansion, exploiting the naive dimensional analysis (NDA) and naturalness, and obtained the G1 and G2 parameter sets. In the Lagrangian density, they considered only the contributions of the isoscalar-isovector cross-coupling, which has a greater implication for the neutron radius and equation of state (EoS) of asymmetric nuclear matter [19]. Later on it was realized that the contributions of δ mesons are also needed to explain certain properties of nuclear phenomena in extreme conditions [20,21]. Though the contributions of the δ mesons to the bulk properties are nominal in normal nuclear matter, the effects are significant for highly asymmetric dense nuclear matter. The δ meson splits the effective masses of proton and neutron, which influences the production of $K^{+,-}$ and π^+/π^- in the heavy-ion collision (HIC) [22]. Also, it increases the proton fraction in the β-stable matter and modifies the transport properties of the neutron star and heavy-ion reactions [23–25]. The source terms for both ρ and δ mesons contain isospin density, but their origins are different. The ρ meson arises from the asymmetry in the number density and the evolution of the δ meson is from the mass asymmetry of the nucleons. The inclusion of δ mesons could influence the certain physical observables like neutron-skin thickness, isotopic shift, two-neutron separation energy S_{2n}, symmetry energy $S(\rho)$, giant dipole resonance, and effective mass of the nucleons, which are correlated with the isovector channel of the interaction. The density dependence of symmetry energy is strongly correlated with the neutron-skin thickness in heavy nuclei, but until now experiments have not fixed the accurate value of the neutron radius, which is under consideration for verification in parity-violating electron-nucleus scattering experiments [18,26].

Recently, the detection of gravitational waves from the binary neutron star GW170817 is a major breakthrough in astrophysics and was detected for the first time by the advanced Laser Interferometer Gravitational-wave Observatory (aLIGO) and advanced VIRGO detectors [27]. This detection has certainly proved to be a valuable guidance to study matter under the most extreme conditions. In-spiraling and coalescing objects of a binary neutron star result in gravitational waves. Due to the merger, a compact remnant remains whose nature is decided by two factors: (i) the masses of the in-spiraling objects and (ii) the equation of state of the neutron star matter. For the final state, the formation of either a neutron star or a black hole depends on the masses and stability of the objects. The chirp mass is measured very precisely from data analysis of GW170817 and it is found to be $1.188^{+0.004}_{-0.002}M_\odot$ for the 90% credible intervals. It is suggested that the total mass should be $2.74^{+0.04}_{-0.01}M_\odot$ for low-spin priors and $2.82^{+0.47}_{-0.09}M_\odot$ for high-spin priors [27]. Moreover, the maximum mass of nonspinning neutron stars (NSs) as a function of radius is observed with the highly precise measurements of $M \approx 2.0M_\odot$. From the observations of gravitational waves, we can extract information regarding the radii or tidal deformability of the nonspinning and spinning NSs [28–30]. Once we succeed in getting this information, it is easy to get the neutron star matter equation of state [31,32].

In the present paper, we constructed a new parameter set, the Institute of Physics Bhubaneswar-I (IOPB-I), using the simulated annealing method (SAM) [33–35] and explored the generic prediction of properties of finite nuclei, nuclear matter, and neutron stars within the E-RMF formalism. Our new parameter set yields the considerable shell gap appearing at neutron numbers $N = 172, 184$, and 198 showing the magicity of these numbers. The behavior of the density-dependent symmetry energy of nuclear matter at low and high densities is examined in detail. The effects of the core EoS on the mass, radius, and tidal deformability of an NS are evaluated using the static $l = 2$ perturbation of a Tolman-Oppenheimer-Volkoff solution.

The paper is organized as follows: In Sec. II, we outline the E-RMF Lagrangian. We outline briefly the equations of motion for finite nuclei and EoS for infinite nuclear matter. In Sec. III, we discuss the strategy of the parameter fitting using the SAM. After getting the new parameter set IOPB-I, the results on binding energy, two-neutron separation energy, and neutron-skin thickness for finite nuclei are discussed in Sec. IV A. In Secs. IV B and IV C, the EoS for symmetric and asymmetric matter are presented. The mass radius and tidal deformability of the neutron star obtained by the new parameter set is also discussed in this section. Finally, the summary and concluding remarks are given in Sec. V. We have taken the value of $G = c = 1$ throughout the paper.

II. FORMALISM

A. Energy density functional and equations of motion

In this section, we outline briefly the E-RMF Lagrangian [1]. The beauty of an effective Lagrangian is that one can ignore the basic difficulties of the formalism, like renormalization and divergence of the system. The model can be used directly by fitting the coupling constants and some masses of the mesons. The E-RMF Lagrangian has an infinite number of terms with all types of self- and cross-couplings. It is necessary to develop a truncation procedure for practical use. Generally, the meson fields constructed in the Lagrangian are smaller than the mass of the nucleon. Their ratio could be used as a truncation scheme as is done in Refs. [1,3,36,37] along with the NDA and naturalness properties. The basic nucleon-meson E-RMF Lagrangian (with δ meson, WR) up to fourth order with exchange mesons like σ, ω, and ρ mesons and photon A is given as [1,38]

$$\mathcal{E}(r) = \sum_\alpha \varphi_\alpha^\dagger(r)\Big\{-i\boldsymbol{\alpha}\cdot\boldsymbol{\nabla} + \beta[M - \Phi(r) - \tau_3 D(r)] + W(r) + \frac{1}{2}\tau_3 R(r) + \frac{1+\tau_3}{2}A(r)$$
$$- \frac{i\beta\boldsymbol{\alpha}}{2M}\cdot\left(f_\omega \boldsymbol{\nabla} W(r) + \frac{1}{2}f_\rho \tau_3 \boldsymbol{\nabla} R(r)\right)\Big\}\varphi_\alpha(r) + \left(\frac{1}{2} + \frac{\kappa_3}{3!}\frac{\Phi(r)}{M} + \frac{\kappa_4}{4!}\frac{\Phi^2(r)}{M^2}\right)\frac{m_s^2}{g_s^2}\Phi^2(r)$$

$$-\frac{\zeta_0}{4!}\frac{1}{g_\omega^2}W^4(r)+\frac{1}{2g_s^2}\left(1+\alpha_1\frac{\Phi(r)}{M}\right)(\nabla\Phi(r))^2-\frac{1}{2g_\omega^2}\left(1+\alpha_2\frac{\Phi(r)}{M}\right)$$
$$\times(\nabla W(r))^2-\frac{1}{2}\left(1+\eta_1\frac{\Phi(r)}{M}+\frac{\eta_2}{2}\frac{\Phi^2(r)}{M^2}\right)\frac{m_\omega^2}{g_\omega^2}W^2(r)-\frac{1}{2e^2}(\nabla A(r))^2-\frac{1}{2g_\rho^2}(\nabla R(r))^2$$
$$-\frac{1}{2}\left(1+\eta_\rho\frac{\Phi(r)}{M}\right)\frac{m_\rho^2}{g_\rho^2}R^2(r)-\Lambda_\omega(R^2(r)W^2(r))+\frac{1}{2g_\delta^2}(\nabla D(r))^2+\frac{1}{2}\frac{{m_\delta}^2}{g_\delta^2}(D^2(r)), \tag{1}$$

where Φ, W, R, D, and A are the fields; g_σ, g_ω, g_ρ, g_δ, and $\frac{e^2}{4\pi}$ are the coupling constants; and m_σ, m_ω, m_ρ, and m_δ are the masses for σ, ω, ρ, and δ mesons and photon, respectively.

Now, our aim is to solve the field equations for the baryons and mesons (nucleon, σ, ω, ρ, and δ) using the variational principle. We obtained the meson equation of motion using the equation $(\frac{\partial\mathcal{E}}{\partial\phi_i})_{\rho=\text{const}}=0$. The single-particle energy for the nucleons is obtained by using the Lagrange multiplier ε_α, which is the energy eigenvalue of the Dirac equation constraining the normalization condition $\sum_\alpha\varphi_\alpha^\dagger(r)\varphi_\alpha(r)=1$ [39]. The Dirac equation for the wave function $\varphi_\alpha(r)$ becomes

$$\frac{\partial}{\partial\varphi_\alpha^\dagger(r)}\left[\mathcal{E}(r)-\sum_\alpha\varphi_\alpha^\dagger(r)\varphi_\alpha(r)\right]=0, \tag{2}$$

i.e.,

$$\left\{-i\boldsymbol{\alpha}\cdot\boldsymbol{\nabla}+\beta[M-\Phi(r)-\tau_3D(r)]+W(r)+\frac{1}{2}\tau_3R(r)+\frac{1+\tau_3}{2}A(r)-\frac{i\beta\boldsymbol{\alpha}}{2M}\cdot\left[f_\omega\nabla W(r)+\frac{1}{2}f_\rho\tau_3\nabla R(r)\right]\right\}\varphi_\alpha(r)$$
$$=\varepsilon_\alpha\,\varphi_\alpha(r). \tag{3}$$

The mean-field equations for Φ, W, R, D, and A are given by

$$-\Delta\Phi(r)+m_s^2\Phi(r)=g_s^2\rho_s(r)-\frac{m_s^2}{M}\Phi^2(r)\left(\frac{\kappa_3}{2}+\frac{\kappa_4}{3!}\frac{\Phi(r)}{M}\right)+\frac{g_s^2}{2M}\left(\eta_1+\eta_2\frac{\Phi(r)}{M}\right)\frac{m_\omega^2}{g_\omega^2}W^2(r)+\frac{\eta_\rho}{2M}\frac{g_s^2}{{g_\rho}^2}m_\rho^2R^2(r)$$
$$+\frac{\alpha_1}{2M}[(\nabla\Phi(r))^2+2\Phi(r)\Delta\Phi(r)]+\frac{\alpha_2}{2M}\frac{g_s^2}{g_\omega^2}(\nabla W(r))^2, \tag{4}$$
$$-\Delta W(r)+m_\omega^2W(r)=g_\omega^2\left(\rho(r)+\frac{f_\omega}{2}\rho_{\mathrm{T}}(r)\right)-\left(\eta_1+\frac{\eta_2}{2}\frac{\Phi(r)}{M}\right)\frac{\Phi(r)}{M}m_\omega^2W(r)-\frac{1}{3!}\zeta_0W^3(r)$$
$$+\frac{\alpha_2}{M}[\nabla\Phi(r)\cdot\nabla W(r)+\Phi(r)\Delta W(r)]-2\,\Lambda_\omega{g_\omega}^2R^2(r)W(r), \tag{5}$$
$$-\Delta R(r)+m_\rho^2R(r)=\frac{1}{2}g_\rho^2\left(\rho_3(r)+\frac{1}{2}f_\rho\rho_{\mathrm{T},3}(r)\right)-\eta_\rho\frac{\Phi(r)}{M}m_\rho^2R(r)-2\,\Lambda_\omega{g_\rho}^2R(r)W^2(r), \tag{6}$$
$$-\Delta A(r)=e^2\rho_{\mathrm{p}}(r), \tag{7}$$
$$-\Delta D(r)+{m_\delta}^2D(r)=g_\delta^2\rho_{s3}, \tag{8}$$

where the baryon, scalar, isovector, proton, and tensor densities are

$$\rho(r)=\sum_\alpha\varphi_\alpha^\dagger(r)\varphi_\alpha(r)=\rho_p(r)+\rho_n(r)=\frac{2}{(2\pi)^3}\int_0^{k_p}d^3k+\frac{2}{(2\pi)^3}\int_0^{k_n}d^3k, \tag{9}$$
$$\rho_s(r)=\sum_\alpha\varphi_\alpha^\dagger(r)\beta\varphi_\alpha(r)=\rho_{sp}(r)+\rho_{sn}(r)=\sum_\alpha\frac{2}{(2\pi)^3}\int_0^{k_\alpha}d^3k\frac{M_\alpha^*}{\left(k_\alpha^2+M_\alpha^{*2}\right)^{\frac{1}{2}}}, \tag{10}$$
$$\rho_3(r)=\sum_\alpha\varphi_\alpha^\dagger(r)\tau_3\varphi_\alpha(r)=\rho_p(r)-\rho_n(r), \tag{11}$$
$$\rho_{s3}(r)=\sum_\alpha\varphi_\alpha^\dagger(r)\tau_3\beta\varphi_\alpha(r)=\rho_{ps}(r)-\rho_{ns}(r) \tag{12}$$
$$\rho_{\mathrm{p}}(r)=\sum_\alpha\varphi_\alpha^\dagger(r)\left(\frac{1+\tau_3}{2}\right)\varphi_\alpha(r), \tag{13}$$
$$\rho_{\mathrm{T}}(r)=\sum_\alpha\frac{i}{M}\boldsymbol{\nabla}\cdot[\varphi_\alpha^\dagger(r)\beta\boldsymbol{\alpha}\varphi_\alpha(r)], \tag{14}$$

and

$$\rho_{\mathrm{T},3}(r) = \sum_{\alpha} \frac{i}{M} \nabla \cdot [\varphi_{\alpha}^{\dagger}(r)\beta\boldsymbol{\alpha}\tau_3\varphi_{\alpha}(r)]. \tag{15}$$

Here k_α is the nucleon's Fermi momentum and the summation is over all the occupied states. The nucleons and mesons are composite particles and their vacuum polarization effects have been neglected. Hence, the negative-energy states do not contribute to the densities and current [11]. In the fitting process, the coupling constants of the effective Lagrangian are determined from a set of experimental data which takes into account the large part of the vacuum polarization effects in the *no-sea approximation*. It is clear that the no-sea approximation is essential to determine the stationary solutions of the relativistic mean-field equations which describe the ground-state properties of the nucleus. The Dirac sea holds the negative-energy eigenvectors of the Dirac Hamiltonian, which is different for different nuclei. Thus, it depends on the specific solution of the set of nonlinear RMF equations. The Dirac spinors can be expanded in terms of vacuum solutions which form a complete set of plane wave functions in spinor space. This set will be complete when the states with negative energies are the part of the positive energy states and create the Dirac sea of the vacuum.

The effective masses of proton, M_p^*, and neutron, M_n^*, are written as

$$M_p^* = M - \Phi(r) - D(r), \tag{16}$$

$$M_n^* = M - \Phi(r) + D(r). \tag{17}$$

The vector potential is

$$V(r) = g_\omega V_0(r) + \frac{1}{2} g_\rho \tau_3 b_0(r) + e\frac{(1-\tau_3)}{2} A_0(r). \tag{18}$$

The set of coupled differential equations is solved self-consistently to describe the ground-state properties of finite nuclei. In the fitting procedure, we used the experimental data of binding energy (BE) and charge radius r_{ch} for a set of spherical nuclei (^{16}O, ^{40}Ca, ^{48}Ca, ^{68}Ni, ^{90}Zr, ^{100,132}Sn, and ^{208}Pb). The total binding energy is obtained by

$$E_{\mathrm{total}} = E_{\mathrm{part}} + E_\sigma + E_\omega + E_\rho + E_\delta + E_{\omega\rho} + E_c + E_{\mathrm{pair}} + E_{c.m.}, \tag{19}$$

where E_{part} is the sum of the single-particle energies of the nucleons and E_σ, E_ω, E_ρ, E_δ, and E_c are the contributions of the respective mesons and Coulomb fields. The pairing E_{pair} and the center of mass motion $E_{c.m.} = \frac{3}{4} \times 41A^{-1/3}$ MeV energies are also taken into account [3,40,41].

The pairing correlation plays a distinct role in open-shell nuclei [42,43]. The effect of the pairing correlation is markedly seen with the increase in mass number A. Moreover, it helps in understanding the deformation of medium and heavy nuclei. It has a lean effect on both bulk and single-particle properties of lighter mass nuclei because of the availability of limited pairs near the Fermi surface. We take the case of the $T = 1$ channel of pairing correlation, i.e., pairing between proton-proton and neutron-neutron. The pairs of nucleons are invariant under time reversal symmetry when the pairing interaction v_{pair} has nonzero matrix elements:

$$\langle \alpha_2 \overline{\alpha_2} | v_{\mathrm{pair}} | \alpha_1 \overline{\alpha_1} \rangle = -G, \tag{20}$$

where $\alpha = |nljm\rangle$ and $\overline{\alpha} = |nlj\,-m\rangle$ (with $G > 0$ and $m > 0$) are the quantum states.

A nucleon of quantum states $|nljm\rangle$ pairs with another nucleon having the same I_z value with quantum states $|nlj\,-m\rangle$, since it is the time reversal partner of the other. In both nuclear and atomic domains, the ideology of BCS pairing is the same. The even-odd mass staggering of isotopes was the first evidence of its kind for the pairing energy. Considering the mean-field formalism the violation of the particle number is seen only due to the pairing correlation. We find terms such as $\varphi^\dagger\varphi$ (density) in the RMF Lagrangian density but we put an embargo on terms of the form $\varphi^\dagger\varphi^\dagger$ or $\varphi\varphi$ since they violate the particle number conservation. Thus, we affirm that BCS calculations have been carried out by a constant gap or constant force approach externally in the RMF model [17,44,45]. In our work, we consider a seniority-type interaction as a tool by taking a constant value of G for pairs of the active pair shell.

The above approach does not go well for nuclei away from the stability line because, in the present case, with the increase in the number of neutrons or protons the corresponding Fermi level goes to zero and the number of available levels above it minimizes. To complement this situation we see that the particle-hole and pair excitations reach the continuum. In Ref. [6] we notice that if we make the BCS calculation using the quasiparticle state as in the Hartree-Fock-Bogoliubov (HFB) calculation, then the BCS binding energies are coming out to be very close to the HFB, but rms radii (i.e., the single-particle wave functions) greatly depend on the size of the box where the calculation is done. This is because of the unphysical neutron (proton) gas in the continuum where wave functions are not confined in a region. The above shortcomings of the BCS approach can be improved by means of the so-called quasibound states, i.e., states bound because of their own centrifugal barrier (centrifugal-plus-Coulomb barrier for protons) [3–5]. Our calculations are done by confining the available space to one harmonic oscillator shell each above and below the Fermi level to exclude the unrealistic pairing of highly excited states in the continuum [3].

B. Nuclear matter properties

1. Energy and pressure density

In static, infinite, uniform, and isotropic nuclear matter, all the gradients of the fields in Eqs. (4)–(8) vanish. By the definition of infinite nuclear matter, the electromagnetic interaction is also neglected. The expressions for energy density and pressure for such a system are obtained from the energy-momentum tensor [46]:

$$T_{\mu\nu} = \sum_i \partial_\nu \phi_i \frac{\partial \mathcal{L}}{\partial(\partial^\mu \phi_i)} - g_{\mu\nu}\mathcal{L}. \tag{21}$$

The zeroth component of the energy-momentum tensor $\langle T_{00}\rangle$ gives the energy density and the third component $\langle T_{ii}\rangle$

computes the pressure of the system [38]:

$$\mathcal{E} = \frac{2}{(2\pi)^3}\int d^3k E_i^*(k) + \rho W + \frac{m_s^2\Phi^2}{g_s^2}\left(\frac{1}{2}+\frac{\kappa_3}{3!}\frac{\Phi}{M}+\frac{\kappa_4}{4!}\frac{\Phi^2}{M^2}\right) - \frac{1}{2}m_\omega^2\frac{W^2}{g_\omega^2}\left(1+\eta_1\frac{\Phi}{M}+\frac{\eta_2}{2}\frac{\Phi^2}{M^2}\right)$$
$$-\frac{1}{4!}\frac{\zeta_0 W^4}{g_\omega^2}+\frac{1}{2}\rho_3 R - \frac{1}{2}\left(1+\frac{\eta_\rho\Phi}{M}\right)\frac{m_\rho^2}{g_\rho^2}R^2 - \Lambda_\omega(R^2W^2)+\frac{1}{2}\frac{m_\delta^2}{g_\delta^2}(D^2), \tag{22}$$

$$P = \frac{2}{3(2\pi)^3}\int d^3k \frac{k^2}{E_i^*(k)} - \frac{m_s^2\Phi^2}{g_s^2}\left(\frac{1}{2}+\frac{\kappa_3}{3!}\frac{\Phi}{M}+\frac{\kappa_4}{4!}\frac{\Phi^2}{M^2}\right)+\frac{1}{2}m_\omega^2\frac{W^2}{g_\omega^2}\left(1+\eta_1\frac{\Phi}{M}+\frac{\eta_2}{2}\frac{\Phi^2}{M^2}\right)$$
$$+\frac{1}{4!}\frac{\zeta_0 W^4}{g_\omega^2}+\frac{1}{2}\left(1+\frac{\eta_\rho\Phi}{M}\right)\frac{m_\rho^2}{g_\rho^2}R^2+\Lambda_\omega(R^2W^2)-\frac{1}{2}\frac{m_\delta^2}{g_\delta^2}(D^2), \tag{23}$$

where $E_i^*(k)=\sqrt{k^2+M_i^{*2}}\,(i=p,n)$ is the energy and k is the momentum of the nucleon. In the context of density functional theory, it is possible to parametrize the exchange and correlation effects through local potentials (Kohn-Sham potentials), as long as those contributions are small enough [47]. The Hartree values control the dynamics in the relativistic Dirac-Brückner-Hartree-Fock calculations. Therefore, the local meson fields in the RMF formalism can be interpreted as Kohn-Sham potentials and in this sense Eqs. (3)–(8) include effects beyond the Hartree approach through the nonlinear couplings [1].

2. Symmetry Energy

The binding energy per nucleon, $\mathcal{E}/A = e(\rho,\alpha)$, can be written in the parabolic form of the asymmetry parameter $\alpha(=\frac{\rho_n-\rho_p}{\rho_n+\rho_p})$:

$$e(\rho,\alpha) = \frac{\mathcal{E}}{\rho_B} - M = e(\rho) + S(\rho)\alpha^2 + \mathcal{O}(\alpha^4), \tag{24}$$

where $e(\rho)$ is energy density of the symmetric nuclear matter (SNM) ($\alpha = 0$) and $S(\rho)$ is defined as the symmetry energy of the system:

$$S(\rho) = \frac{1}{2}\left[\frac{\partial^2 e(\rho,\alpha)}{\partial\alpha^2}\right]_{\alpha=0}. \tag{25}$$

The isospin asymmetry arises due to the difference in densities and masses of the neutron and proton. The density-type isospin asymmetry is taken care by the ρ meson (isovector-vector meson) and mass asymmetry by the δ meson (isovector-scalar meson). The general expression for symmetry energy $S(\rho)$ is a combined expression of ρ and δ mesons, which is defined as [3,20,48,49]

$$S(\rho) = S^{\rm kin}(\rho) + S^{\rho}(\rho) + S^{\delta}(\rho), \tag{26}$$

with

$$S^{\rm kin}(\rho) = \frac{k_F^2}{6E_F^*}, \quad S^{\rho}(\rho) = \frac{g_\rho^2\rho}{8m_\rho^{*2}}, \tag{27}$$

and

$$S^{\delta}(\rho) = -\frac{1}{2}\rho\frac{g_\delta^2}{m_\delta^2}\left(\frac{M^*}{E_F}\right)^2 u_\delta(\rho,M^*). \tag{28}$$

The last function u_δ is from the discreteness of the Fermi momentum. This momentum is quite large in nuclear matter and can be treated as a continuum and continuous system. The function u_δ is defined as

$$u_\delta(\rho,M^*) = \frac{1}{1+3\frac{g_\delta^2}{m_\delta^2}\left(\frac{\rho^s}{M^*}-\frac{\rho}{E_F}\right)}. \tag{29}$$

In the limit of continuum, the function $u_\delta \approx 1$. The whole symmetry energy ($S^{\rm kin}+S^{\rm pot}$) arises from ρ and δ mesons and is given as

$$S(\rho) = \frac{k_F^2}{6E_F^*}+\frac{g_\rho^2\rho}{8m_\rho^{*2}}-\frac{1}{2}\rho\frac{g_\delta^2}{m_\delta^2}\left(\frac{M^*}{E_F}\right)^2, \tag{30}$$

where E_F^* is the Fermi energy and k_F is the Fermi momentum. The mass of the ρ meson is modified because of the cross-coupling of ρ-ω fields and is given by

$$m_\rho^{*2} = \left(1+\eta_\rho\frac{\Phi}{M}\right)m_\rho^2 + 2g_\rho^2(\Lambda_\omega W^2). \tag{31}$$

The cross-coupling of isoscalar-isovector mesons (Λ_ω) modifies the density dependence of $S(\rho)$ without affecting the saturation properties of the SNM [26,50]. In the numerical calculation, the coefficient of symmetry energy $S(\rho)$ is obtained by the energy difference of symmetric and pure neutron matter at saturation. In our calculation, we have taken the isovector channel into account to make the new parameters, which incorporate the currently existing experimental observations, and predictions are made keeping in mind some future aspects of the model. The symmetry energy can be expanded as a Taylor series around the saturation density ρ_0 as

$$S(\rho) = J + L\mathcal{Y} + \tfrac{1}{2}K_{\rm sym}\mathcal{Y}^2 + \tfrac{1}{6}Q_{\rm sym}\mathcal{Y}^3 + \mathcal{O}[\mathcal{Y}^4], \tag{32}$$

where $J = S(\rho_0)$ is the symmetry energy at saturation and $\mathcal{Y} = \frac{\rho-\rho_0}{3\rho_0}$. The coefficients $L(\rho_0)$, $K_{\rm sym}(\rho_0)$, and $Q_{\rm sym}$ are defined as

$$L = 3\rho\frac{\partial S(\rho)}{\partial\rho}\bigg|_{\rho=\rho_0}, \tag{33}$$

$$K_{\rm sym} = 9\rho^2\frac{\partial^2 S(\rho)}{\partial\rho^2}\bigg|_{\rho=\rho_0}, \tag{34}$$

$$Q_{\rm sym} = 27\rho^3\frac{\partial^3 S(\rho)}{\partial\rho^3}\bigg|_{\rho=\rho_0}. \tag{35}$$

Similarly, we obtain the asymmetric nuclear matter incompressibility as $K(\alpha) = K + K_\tau\alpha^2 + \mathcal{O}(\alpha^4)$ and K_τ is given

by [51]

$$K_\tau = K_{\rm sym} - 6L - \frac{Q_0 L}{K}, \tag{36}$$

where $Q_0 = 27\rho^3 \frac{\partial^3(\mathcal{E}/\rho)}{\partial\rho^3}$ in SNM.

Here, L is the slope and $K_{\rm sym}$ represents the curvature of $S(\rho)$ at saturation density. A large number of investigations have been made to fix the values of J, L, and $K_{\rm sym}$ [50,52–57]. The density dependence of symmetry energy is a key quantity to control the properties of both finite nuclei and infinite nuclear matter [58]. Currently, the available information on symmetry energy $J = 31.6 \pm 2.66$ MeV and its slope $L = 58.9 \pm 16$ MeV at saturation density are obtained by various astrophysical observations [59]. To date, the precise values of J, L, and the neutron radii for finite nuclei are not known experimentally; it is essential to discuss the behavior of the symmetry energy as a function of density in our new parameter set.

III. PARAMETER FITTING

The SAM is used to determine the parameters used in the Lagrangian density [60,61]. The SAM is useful in the global minimization technique; i.e., it gives accurate results when there exists a global minimum within several local minima. Usually, this procedure is used in a system in which the number of parameters is more than the number of observables [62–64]. In this simulation method, the system stabilizes when the temperature T (a variable which controls the energy of the system) goes down [33–35]. Initially, the nuclear system is put at a high temperature (highly unstable) and then allowed to cool down slowly so that it is stabilized in a very smooth way and finally reaches the frozen temperature (stable or systematic system). The variation of T should be very small near the stable state. The $\chi^2 = \chi^2(p_1, \ldots, p_N)$ values of the considered systems are minimized (least-squares fit), which is governed by the model parameters p_i. The general expression of χ^2 can be given as

$$\chi^2 = \frac{1}{N_d - N_p} \sum_{i=1}^{N_d} \left(\frac{M_i^{\rm expt} - M_i^{th}}{\sigma_i} \right)^2. \tag{37}$$

Here, N_d and N_p are the numbers of experimental data points and fitting parameters, respectively. The experimental and theoretical values of the observables are denoted by $M_i^{\rm expt}$ and M_i^{th}, respectively. The σ_i's are the adopted errors [65]. The adopted errors are composed of three components, namely, the experimental, numerical, and theoretical errors [65]. As the name suggests, the experimental errors are associated with the measurements; numerical and theoretical errors are associated with the numerics and the shortcomings of the nuclear model employed, respectively. In principle, there exists some arbitrariness in choosing the values of σ_i, which is partially responsible for the proliferation of the mean-field models. The only guidance available from the statistical analysis is that the χ^2 per degree of freedom [Eq. (37)] should be close to unity. In the present calculation, we used some selected fit data for binding energy and the root mean square radius of the charge distribution for some selected nuclei and the associated adopted errors on them [66].

TABLE I. The obtained new parameter set IOPB-I along with NL3 [13], FSUGarnet [67], and G3 [21] sets. The nucleon mass M is 939.0 MeV. All the coupling constants are dimensionless except k_3, which is in fm^{-1}.

	NL3	FSUGarnet	G3	IOPB-I
m_s/M	0.541	0.529	0.559	0.533
m_ω/M	0.833	0.833	0.832	0.833
m_ρ/M	0.812	0.812	0.820	0.812
m_δ/M	0.0	0.0	1.043	0.0
$g_s/4\pi$	0.813	0.837	0.782	0.827
$g_\omega/4\pi$	1.024	1.091	0.923	1.062
$g_\rho/4\pi$	0.712	1.105	0.962	0.885
$g_\delta/4\pi$	0.0	0.0	0.160	0.0
k_3	1.465	1.368	2.606	1.496
k_4	−5.688	−1.397	1.694	−2.932
ζ_0	0.0	4.410	1.010	3.103
η_1	0.0	0.0	0.424	0.0
η_2	0.0	0.0	0.114	0.0
η_ρ	0.0	0.0	0.645	0.0
Λ_ω	0.0	0.043	0.038	0.024
α_1	0.0	0.0	2.000	0.0
α_2	0.0	0.0	−1.468	0.0
$f_\omega/4$	0.0	0.0	0.220	0.0
$f_\rho/4$	0.0	0.0	1.239	0.0
β_σ	0.0	0.0	−0.087	0.0
β_ω	0.0	0.0	−0.484	0.0

In our calculations, we have built a new parameter set IOPB-I and analyzed its effects for finite and infinite nuclear systems. Thus, we performed an overall fit with eight parameters, where the nucleons as well as the masses of the two vector mesons in free space are fixed at their experimental values, i.e., $M = 939$ MeV, $m_\omega = 782.5$ MeV, and $m_\rho = 763.0$ MeV. The effective nucleon mass can be used as a nuclear matter constraint at the saturation density ρ_0 along with other empirical values like incompressibility, binding energy per nucleon, and asymmetric parameter J. While fitting the parameter, the values of effective nucleon mass M^*/M, nuclear matter incompressibility K, and symmetry energy coefficient J are constrained within 0.50–0.90, 220–260, and 28–36 MeV, respectively. The minimum χ^2 is obtained by the simulated annealing method [33–35] to fix the final parameters. The newly developed IOPB-I set along with NL3 [13], FSUGarnet [67], and G3 [21] are given for comparison in Table I. The calculated results of the binding energy and charge radius are compared with the known experimental data [68,69]. It is to be noted that in the original E-RMF parametrization, only five spherical nuclei were taken into consideration while fitting the parameters with the binding energy, charge radius, and single-particle energy [1]. However, here, eight spherical nuclei are used for the fitting as listed in Table II.

IV. RESULTS AND DISCUSSIONS

In this section we discuss our calculated results for finite nuclei, infinite nuclear matter, and neutron stars. For finite

TABLE II. The calculated binding energy per particle (B/A) and charge radius (R_c) are compared with the available experimental data [68,69]. The predicted neutron-skin thickness $\Delta r_{np} = R_n - R_p$ is also depicted for all four models.

Nucleus	Obs.	Expt.	NL3	FSUGarnet	G3	IOPB-I
^{16}O	B/A	7.976	7.917	7.876	8.037	7.977
	R_c	2.699	2.714	2.690	2.707	2.705
	$R_n - R_p$		−0.026	−0.028	−0.028	−0.027
^{40}Ca	B/A	8.551	8.540	8.528	8.561	8.577
	R_c	3.478	3.466	3.438	3.459	3.458
	$R_n - R_p$		−0.046	−0.051	−0.049	−0.049
^{48}Ca	B/A	8.666	8.636	8.609	8.671	8.638
	R_c	3.477	3.443	3.426	3.466	3.446
	$R_n - R_p$		0.229	0.169	0.174	0.202
^{68}Ni	B/A	8.682	8.698	8.692	8.690	8.707
	R_c		3.870	3.861	3.892	3.873
	$R_n - R_p$		0.262	0.184	0.190	0.223
^{90}Zr	B/A	8.709	8.695	8.693	8.699	8.691
	R_c	4.269	4.253	4.231	4.276	4.253
	$R_n - R_p$		0.115	0.065	0.068	0.091
^{100}Sn	B/A	8.258	8.301	8.298	8.266	8.284
	R_c		4.469	4.426	4.497	4.464
	$R_n - R_p$		−0.073	−0.078	−0.079	−0.077
^{132}Sn	B/A	8.355	8.371	8.372	8.359	8.352
	R_c	4.709	4.697	4.687	4.732	4.706
	$R_n - R_p$		0.349	0.224	0.243	0.287
^{208}Pb	B/A	7.867	7.885	7.902	7.863	7.870
	R_c	5.501	5.509	5.496	5.541	5.521
	$R_n - R_p$		0.283	0.162	0.180	0.221

nuclei, binding energy, rms radii for neutron and proton distributions, two-neutron separation energy, and neutron-skin thickness are analyzed. Similarly, for infinite nuclear matter systems, the binding energies per particle for symmetric and asymmetric nuclear matter including pure neutron matter at both subsaturation and suprasaturation densities are compared with other theoretical results and experimental data. The parameter set IOPB-I is also applied to study the structure of neutron stars using β equilibrium and charge neutrality conditions.

A. Finite nuclei

1. Binding energies, charge radii, and neutron-skin thickness

We used eight spherical nuclei to fit the experimental ground-state binding energies and charge radii using the SAM. The calculated results are listed in Table II and compared with other theoretical models as well as experimental data [68,69]. It can be seen that the NL3 [13], FSUGarnet [67], and G3 [21] models successfully reproduce the energies and charge radii as well. Even though the "mean-field models are not expected to work well for the light nuclei," the results deviate only marginally for the ground-state properties for light nuclei [70]. We noticed that both the binding energy and charge radius of ^{16}O are well produced by IOPB-I. However, the charge radii

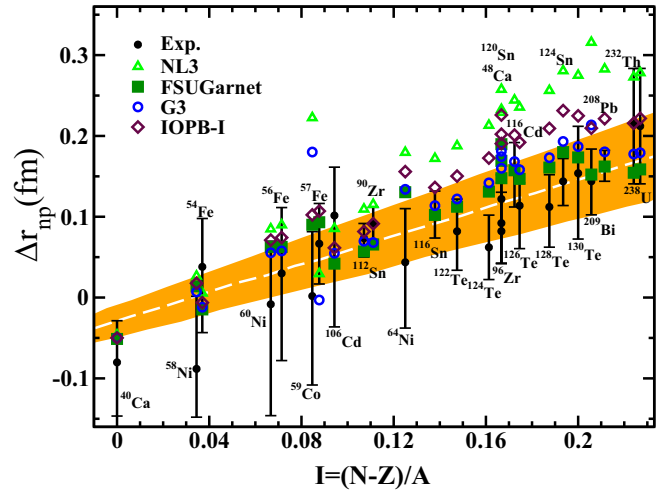

FIG. 1. The neutron-skin thickness as a function of the asymmetry parameter. Results obtained with the parameter set IOPB-I are compared with those of the sets NL3 [13], FSUGarnet [67], G3 [21], and experimental values [76]. The shaded region is calculated using Eq. (39).

of ^{40,48}Ca slightly underestimate the data. We would like to emphasize that it is an open problem to mean-field models to predict the evolution of charge radii of $^{38-52}$Ca (see Fig. 3 in Ref. [71]).

The excess of neutrons gives rise to a neutron-skin thickness. The neutron-skin thickness Δr_{np} is defined as

$$\Delta r_{np} = \langle r^2 \rangle_n^{1/2} - \langle r^2 \rangle_p^{1/2} = R_n - R_p, \tag{38}$$

with R_n and R_p being the rms radii for the neutron and proton distributions, respectively. The Δr_{np}, strongly correlated with the slope of the symmetry energy [72–74], can probe the isovector part of the nuclear interaction. However, there is a large uncertainty in the experimental measurement of the neutron distribution radius of the finite nuclei. The current values of neutron radius and neutron-skin thickness of ^{208}Pb are $5.78^{+0.16}_{-0.18}$ and $0.33^{+0.16}_{-0.18}$ fm, respectively [75]. This error bar is too large to provide significant constraints on the density-dependent symmetry energy. It is expected that PREX-II result will give us the neutron radius of ^{208}Pb within 1% accuracy. The inclusion of some isovector-dependent terms in the Lagrangian density is needed, which would provide the freedom to refit the coupling constants within the experimental data without compromising the quality of fit. The addition of ω-ρ cross-coupling into the Lagrangian density controls the neutron-skin thickness of ^{208}Pb as well as that of other nuclei. In Fig. 1, we show the neutron-skin thickness Δr_{np} for ^{40}Ca to ^{238}U nuclei as a function of proton-neutron asymmetry $I = (N - Z)/A$. The calculated results of Δr_{np} for NL3, FSUGarnet, G3, and IOPB-I parameter sets are compared with the corresponding experimental data [76]. Experiments have been done with antiprotons at CERN and the Δr_{np} are extracted for 26 stable nuclei ranging from ^{40}Ca to ^{238}U as displayed in the figure along with the error bars. The trend of the data points shows approximately linear dependence of neutron-skin thickness on the relative neutron excess I of a nucleus that can be fitted

by [76,77]:

$$\Delta r_{np} = (0.90 \pm 0.15)I + (-0.03 \pm 0.02)\ \text{fm}. \quad (39)$$

The values of Δr_{np} obtained with IOPB-I for some of the nuclei slightly deviate from the shaded region, as can be seen from Fig. 1. This is because IOPB-I has a smaller strength of ω-ρ cross-coupling as compared to the FSUGarnet set. Recently, Fattoyev *et al.* constrained the upper limit of $\Delta r_{np} \lesssim 0.25$ fm for the ^{208}Pb nucleus with the help of GW170817 observation data [78]. The calculated values of neutron-skin thickness for the ^{208}Pb nucleus are 0.283, 0.162, 0.180, and 0.221 fm for the NL3, FSUGarnet, G3, and IOPB-I parameter sets, respectively. The proton elastic scattering experiment recently measured neutron-skin thickness $\Delta r_{np} = 0.211^{+0.054}_{-0.063}$ fm for ^{208}Pb [79]. Thus values of $\Delta r_{np} = 0.221$ for IOPB-I are consistent with the recent prediction of neutron-skin thickness.

2. Two-neutron separation energy $S_{2n}(Z,N)$

The large shell gap in single-particle energy levels is an indication of the magic number. This is responsible for the extra stability for the magic nuclei. The extra stability for a particular nucleon number can be understood from the sudden fall in the two-neutron separation energy S_{2n}. The S_{2n} can be estimated by the difference in ground-state binding energies of two isotopes, i.e.,

$$S_{2n}(Z,N) = BE(Z,N) - BE(Z,N-2). \quad (40)$$

In Fig. 2, we display results for the S_{2n} as a function of neutron numbers for Ca, Ni, Zr, Sn, Pb, and $Z = 120$ isotopic chains. The calculated results are compared with the finite range droplet model (FRDM) [80] and the most recent experimental data [68]. From the figure, it is clear that there is an evolution of magicity as one moves from the valley of stability to the drip line. In all cases, the S_{2n} values decrease gradually with increase in neutron number. The experimental manifestation of large shell gaps at neutron numbers $N = 20$, 28 (Ca), 28 (Ni), 50 (Zr), 82 (Sn), and 126(Pb) are reasonably well reproduced by the four relativistic sets. Figure 2 shows that the experimental S_{2n} of $^{50-52}$Ca are in good agreement with the prediction of the NL3 set. It is interesting to note that all sets predict the subshell closure at $N = 40$ for Ni isotopes. Furthermore, the two-neutron separation energy for the isotopic chain of nuclei with $Z = 120$ is also displayed in Fig. 2. For the isotopic chain of $Z = 120$, no experimental information exists. The only comparison can be made with theoretical models such as the FRDM [68]. At $N = 172$, 184, and 198 sharp falls in separation energy are seen for all forces, which have been predicted by various theoretical models in the superheavy mass region [81–84]. It is to be noted that the isotopes with $Z = 120$ are shown to be spherical in their ground state [84]. In a detailed calculation, Bhuyan and Patra, using both RMF and Skyrme-Hartree-Fock formalisms, predicted that $Z = 120$ could be the next magic number after $Z = 82$ in the superheavy region [85]. Thus, the deformation effects may not affect the results for $Z = 120$. Therefore, a future mass measurement of ^{292,304,318}120 would confirm a key test for the theory, as well as direct information about the closed-shell behavior at $N = 172$, 184, and 198.

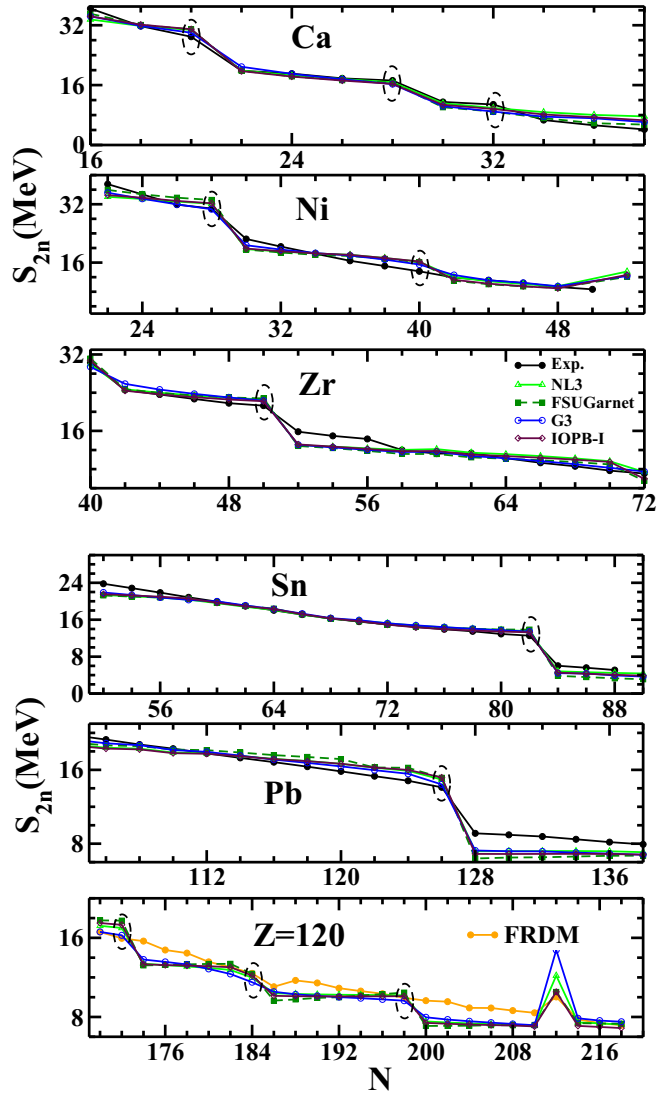

FIG. 2. The two-neutron separation energy as a function of neutron number for the isotopic series of Ca, Ni, Zr, Sn, and Pb nuclei with NL3 [13], FSUGarnet [67], G3 [21], FRDM [80], and experimental data [68] whenever available. The dotted circle represents the magicity of the nuclei.

B. Infinite nuclear matter

The nuclear incompressibility K determines the extent to which the nuclear matter can be compressed. This plays an important role in the nuclear EoS. Currently, the accepted value of $K = 240 \pm 20$ MeV was determined from isoscalar giant monopole resonance (ISGMR) for ^{90}Zr and ^{208}Pb nuclei [86,87]. For our parameter set IOPB-I, we get $K = 222.65$ MeV. The density-dependent symmetry energy $S(\rho)$ is determined from Eq. (32) using IOPB-I along with three adopted models. The calculated results of the symmetry energy coefficient (J), the slope of symmetry energy (L), and other saturation properties are listed in Table III. We find that in case of IOPB-I, $J = 33.3$ MeV and $L = 63.6$ MeV. These values are compatible with $J = 31.6 \pm 2.66$ MeV and

TABLE III. The nuclear matter properties such as binding energy per nucleon, $\mathcal{E}_0$ (MeV), saturation density ρ_0 (fm^{-3}), incompressibility coefficient for symmetric nuclear matter K (MeV), effective mass ratio M^*/M, symmetry energy J (MeV), and linear density dependence of the symmetry energy, L (MeV), at saturation.

	NL3	FSUGarnet	G3	IOPB-I
ρ_0 (fm^{-3})	0.148	0.153	0.148	0.149
$\mathcal{E}_0$ (MeV)	−16.29	−16.23	−16.02	−16.10
M^*/M	0.595	0.578	0.699	0.593
J (MeV)	37.43	30.95	31.84	33.30
L (MeV)	118.65	51.04	49.31	63.58
$K_{\rm sym}$ (MeV)	101.34	59.36	−106.07	−37.09
$Q_{\rm sym}$ (MeV)	177.90	130.93	915.47	862.70
K (MeV)	271.38	229.5	243.96	222.65
Q_0 (MeV)	211.94	15.76	−466.61	−101.37
K_τ (MeV)	−703.23	−250.41	−307.65	−389.46
$K_{\rm asy}$ (MeV)	−610.56	−246.89	−401.97	−418.58
$K_{\rm sat2}$ (MeV)	−703.23	−250.41	−307.65	−389.46

$L = 58.9 \pm 16$ MeV obtained by various terrestrial experimental information and astrophysical observations [59].

Another important constraint K_τ has been suggested which lies in the range of −840 to −350 MeV [88–90] by various experimental data on isoscalar giant monopole resonance, which we can calculate from Eq. (36). It is to be noticed that the calculated values of K_τ are −703.23, −250.41, −307.65, and −389.46 MeV for NL3, FSUGarnet, G3, and IOPB-I parameter sets, respectively. The ISGMR measurement was investigated in a series of $^{112-124}$Sn isotopes, which extracted the value of $K_\tau = -395 \pm 40$ MeV [91]. It is found that $K_\tau = -389.46$ MeV for the IOPB-I set is consistent with GMR measurements [91]. In the absence of cross-coupling, $S(\rho)$ of NL3 is stiffer at low- and high-density regimes, as displayed in Fig. 3. Alternatively, the presence of cross-coupling of ρ mesons to the ω (in the case of FSUGarnet and IOPB-I) and σ mesons (in case of G3) yields the softer symmetry energy at low density, which is consistent with HIC Sn+Sn [93] and IAS [92] data as shown in the figure. However, the IOPB-I set has softer $S(\rho)$ in comparison to the NL3 parameter set at higher density, which lies inside the shaded region of ASY-EoS experimental data [94].

Next, we display in Fig. 4 the binding energy per neutron (B/N) as a function of the neutron density. Here, special attention is needed to build a nucleon-nucleon interaction to fit the data at subsaturation density. For example, the EoS of pure neutron matter (PNM) at low density is obtained within the variational method, which is obtained with an Urbana $v14$ interaction [96]. In this regard, the effective mean-field models also fulfill this demand to some extent [21,67,100]. The cross-coupling ω-ρ plays an important role at low density of the PNM. The low-density (zoomed pattern) nature of the FSUGarnet, G3, and IOPB-I sets are in harmony with the results obtained by microscopic calculations [53,95–98], while the results for NL3 deviate from the shaded region at low- as well as high-density regions. We also find a very good agreement for FSUGarnet, G3, and IOPB-I sets at higher densities, which have been obtained with chiral two-nucleon (NN) and three-nucleon ($3N$) interactions [99].

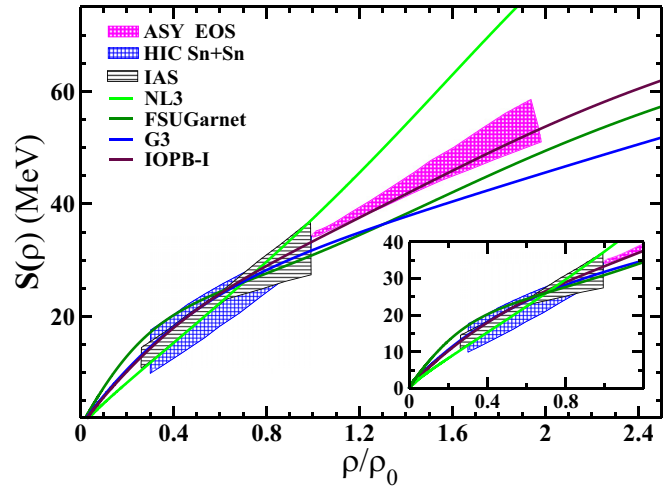

FIG. 3. Density-dependent symmetry energy from Eq. (32) with different E-RMF parameter sets along with IOPB-I parametrization. The shaded region is the symmetry energy from IAS [92], HIC Sn+Sn [93], and ASY-EoS experimental data [94]. The zoomed pattern of the symmetry energy at low densities is shown in the inset.

In Fig. 5, we show the calculated pressure P for the SNM and PNM with the baryon density for the four E-RMF models, which then are compared with the experimental flow data [101]. It is seen from Fig. 5(a) that the SNM EoS for the G3 parameter set is in excellent agreement with the flow data for the entire density range. The SNM EoS for the FSUGarnet and IOPB-I parameter sets are also compatible

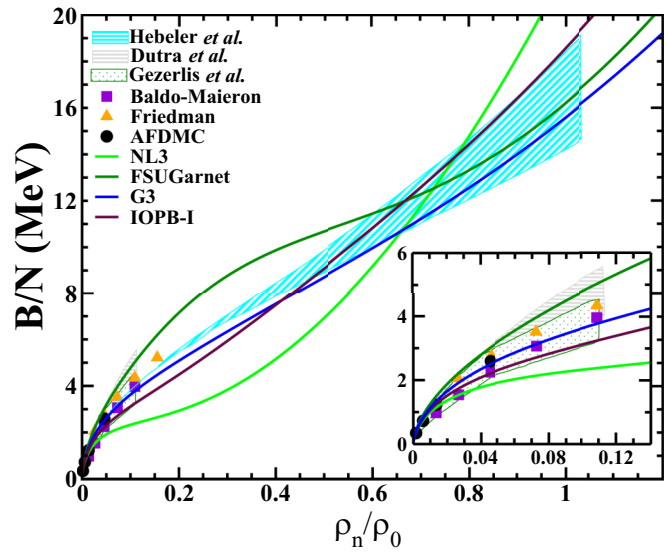

FIG. 4. The energy per neutron as a function of neutron density with NL3 [13], FSUGarnet [67], G3 [21], and IOPB-I parameter sets. Other curves and shaded regions represent the results for various microscopic approaches such as Baldo-Maieron [95], Friedman [96], auxiliary-field diffusion Monte Carlo [97], Dutra [53], Gezerlis [98], and Hebeler [99] methods.

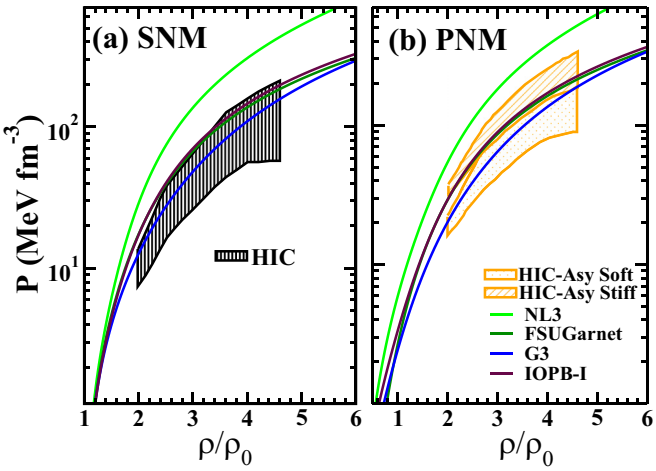

FIG. 5. Pressure as a function of baryon density for the IOPB-I force. The results with NL3 [13], FSUGarnet [67], and G3 [21], are compared with the EoS extracted from the analysis [101] for the (a) symmetric nuclear matter (SNM) and (b) pure neutron matter (PNM).

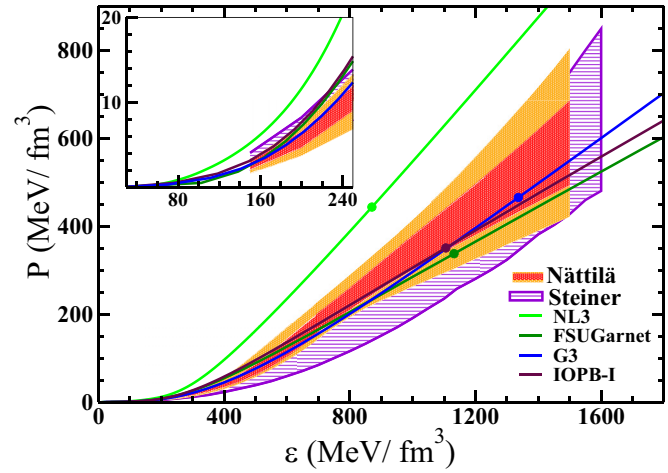

FIG. 6. The equations of statewith NL3, FSUGarnet, G3, and IOPB-I sets for nuclear matter under charge neutrality as well as the β-equilibrium condition. The shaded region (violet) represents the observational constraint at $r_{ph} = R$ with uncertainty of 2σ [104]. Here, R and r_{ph} are the neutron star radius and the photospheric radius, respectively. The other shaded region (red and orange) represents the QMC+Model A equation of state of cold dense matter with 95% confidence limit [103]. The region zoomed near the origin is shown in the inset.

with the experimental HIC data but they are stiffer relative to the EoS for the G3 parametrization. In Fig. 5(b), the bounds on the PNM EoS are divided into two categories: (i) the upper one corresponds to a strong density dependence of symmetry energy $S(\rho)$ (HIC-Asy Stiff) and (ii) the lower one corresponds to the weakest $S(\rho)$ (HIC-Asy Soft) [101,102]. Our parameter set IOPB-I along with the G3 and FSUGarnet sets are reasonably in good agreement with experimental flow data. The PNM EoS for the IOPB-I model is quite stiffer than that of G3 at high densities.

C. Neutron stars

1. Predicted equation of states

We have solved Eqs. (22) and (23) for the energy density and pressure of the β-equilibrated charge neutral neutron star matter. Figure 6 displays the pressure as a function of energy density for the IOPB-I set along with the NL3, FSUGarnet, and G3 sets. The solid circles are the central pressure and energy density corresponding to the maximum mass of the neutron star obtained from the above equations of state. The shaded region of the EoS can be divided into two parts as follows:

(i) Nättliä *et al.* applied the Bayesian cooling tail method to constrain (1σ and 2σ confidence limit) the EoS of cold dense matter inside the neutron stars [103].
(ii) Steiner *et al.* determined an empirical dense matter EoS with a 95% confidence limit from a heterogeneous data set containing PRE bursts and quiescent thermal emission from x-ray transients [104].

From Fig. 6, it is clear that IOPB-I and FSUGarnet EoSs are similar at high density but they differ remarkably at low densities as shown in the zoomed area of the inset. The NL3 set yields the stiffer EoS. Moreover, the IOPB-I set shows the stiffest EoS up to energy densities $\mathcal{E} \lesssim 700$ MeV fm^{-3}. It can be seen that the results of IOPB-I at very high densities $\mathcal{E} \sim$ 400–1600 MeV fm^{-3} are consistent with the EoS obtained by Nättilä *et al.* and Steiner *et al.* [103,104]. However, the FSUGarnet set has a softer EoS at low energy densities $\mathcal{E} \lesssim$ 200 MeV fm^{-3} and stiffer EoS at intermediate energy densities as compared to that for the G3 set. One can conclude from Table III that the symmetry energy elements L and $K_{\rm sym}$ are smaller in the G3 model compared to the IOPB-I, FSUGarnet, and NL3 sets. Hence, it yields the symmetry energy that is softer at higher density.

2. Mass radius and tidal deformability of neutron star

After fixing the equation of state for the various parameter sets, we extended our study to calculate the mass, radius, and tidal deformability of a nonrotating neutron star. Placing a spherical star in a static external quadrupolar tidal field $\mathcal{E}_{ij}$ results in deformation of the star along with quadrupole deformation, which is the leading order perturbation. Such a deformation is measured by [30]

$$\lambda = -\frac{Q_{ij}}{\mathcal{E}_{ij}} = \frac{2}{3}k_2 R^5, \tag{41}$$

$$\Lambda = \frac{2k_2}{3C^5}, \tag{42}$$

where Q_{ij} is the induced quadrupole moment of a star in binary, and $\mathcal{E}_{ij}$ is the static external quadrupole tidal field of the companion star. λ is the tidal deformability parameter depending on the EoS via both the NS radius and a dimensionless quantity k_2, called the second Love number [28,30]. Λ is the dimensionless version of λ, and C is the compactness parameter ($C = M/R$). However, in general relativity (GR) we have to distinguish k_2 between gravitational fields generated by masses (electric type) and those generated by the motion of masses, i.e., mass currents (magnetic type) [32,105]. The electric tidal Love number is

found from the following expression [30]:

$$k_2 = \frac{8}{5}(1-2C)^2C^5[2C(y-1)-y+2]\Big\{2C(4(y+1)C^4 + (6y-4)C^3 + (26-22y)C^2 + 3(5y-8)C - 3y + 6) - 3(1-2C)^2(2C(y-1)-y+2)\log\left(\frac{1}{1-2C}\right)\Big\}^{-1}. \quad (43)$$

The value of $y \equiv y(R)$ can be computed by solving the following first order differential equation [29,32]:

$$r\frac{dy(r)}{dr} + y(r)^2 + y(r)F(r) + r^2Q(r) = 0, \quad (44)$$

with

$$F(r) = \frac{r - 4\pi r^3[\mathcal{E}(r) - P(r)]}{r - 2M(r)}, \quad (45)$$

$$Q(r) = \frac{4\pi r\left(5\mathcal{E}(r) + 9P(r) + \frac{\mathcal{E}(r)+P(r)}{\partial P(r)/\partial\mathcal{E}(r)} - \frac{6}{4\pi r^2}\right)}{r - 2M(r)} - 4\left[\frac{M(r) + 4\pi r^3 P(r)}{r^2(1-2M(r)/r)}\right]^2. \quad (46)$$

To estimate the tidal deformability λ of a single star, Eq. (44) must be integrated simultaneously with the Tolman-Oppenheimer-Volkov equations [106], i.e.,

$$\frac{dP(r)}{dr} = -\frac{[\mathcal{E}(r) + P(r)][M(r) + 4\pi r^3 P(r)]}{r^2\left(1 - \frac{2M(r)}{r}\right)}, \quad (47)$$

and

$$\frac{dM(r)}{dr} = 4\pi r^2\mathcal{E}(r). \quad (48)$$

For a given EoS and from the boundary conditions $P(0) = P_c$, $M(0) = 0$, and $y(0) = 2$, where P_c, $M(0)$, and $y(0)$ are the central pressure, mass, and dimensionless quantity. To obtain the tidal Love number, we solve this set of Eqs. (41)–(48) for a given EoS of the star at $r = 0$. The value of $r(=R)$ where the pressure vanishes defines the surface of the star. Thus, at each central density we can uniquely determine a mass M, a radius R, and a tidal Love number k_2 of the isolated neutron star using the chosen EoS. In Fig. 7, the horizontal bars in cyan and magenta include the results from the precisely measured neutron stars masses, such as PSR J1614-2230 with mass $M = 1.97 \pm 0.04 M_\odot$ [107] and PSR J0348+0432 with $M = 2.01 \pm 0.04 M_\odot$ [108]. These observations imply that the maximum mass predicted by any theoretical model should reach the limit $\sim 2.0 M_\odot$. We also depict the 1σ and 2σ empirical mass-radius constraints for the cold dense matter inside the NS, which were obtained from a Bayesian analysis of type-I x-ray burst observations [103]. A similar approach was applied by Steiner *et al.*, but they obtained the mass radius from six sources, i.e., three from transient low-mass x-ray binaries and three from type-I x-ray bursters with photospheric radius [104].

The NL3 model of RMF theory suggests a larger and massive NS with mass $2.77 M_\odot$ and the corresponding NS radius to be 13.314 km, which is larger than the best observational radius

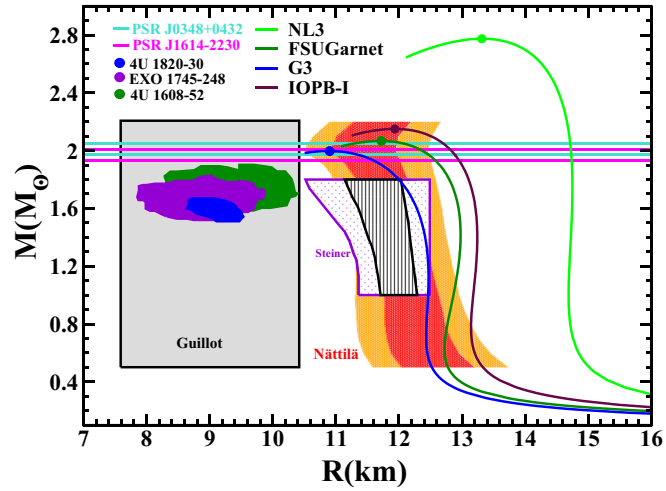

FIG. 7. The mass-radius profile predicted by NL3, FSUGarnet, G3, and IOPB-I parameter sets. The recent observational constraints on neutron-star masses [107,108] and radii [103,104,116,117] are also shown.

estimates [103,104]. Hence it is clear that the new RMF was developed either through density-dependent couplings [49] or higher order couplings [21,67]. These models successfully reproduce the ground-state properties of finite nuclei, nuclear matter saturation properties, and also the maximum mass of the neutron stars. Another important advantage of these models is that they are consistent with the subsaturation density of the pure neutron matter. Rezzolla *et al.* [109] combined the recent gravitational-wave observation of a merging system of binary neutron stars via the event GW170817 with quasi-universal relations between the maximum mass of rotating and nonrotating NSs. It is found that the maximum mass for a nonrotating NS should be in the range $2.01 \pm 0.04 \lesssim M(M_\odot) \lesssim 2.16 \pm 0.03$ [109], where the lower limit is observed from massive pulsars in the binary system [108]. From the results, we find that the maximum masses for IOPB-I along with FSUGarnet and G3 EoS are consistent with the observed lower bound on the maximum NS mass. For the IOPB-I parametrization,

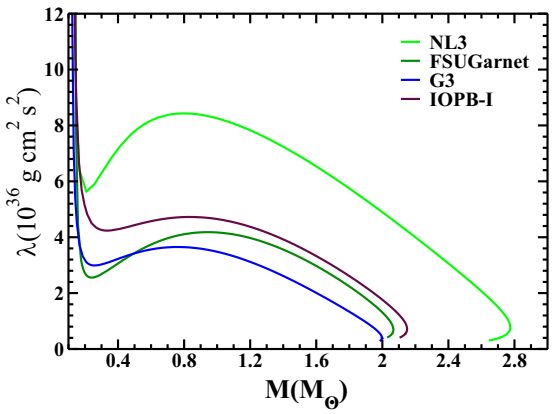

FIG. 8. The tidal deformability λ as a function of neutron star mass with different EoS.

TABLE IV. The binary neutron star masses ($m_1(M_\odot)$,$m_2(M_\odot)$) and corresponding radii (R_1 (km), R_2 (km)), tidal Love number ($(k_2)_1$, $(k_2)_2$), and tidal deformabilities (λ_1,λ_2) in 1×10^{36} g cm^2 s^2 and dimensionless tidal deformabilities (Λ_1,Λ_2). $\tilde{\Lambda}$, $\delta\tilde{\Lambda}$, $\mathcal{M}_c(M_\odot)$, and $\mathcal{R}_c(km)$ are the dimensionless tidal deformability, tidal correction, chirp mass, and radius of the binary neutron star, respectively.

EoS	$m_1(M_\odot)$	$m_2(M_\odot)$	R_1 (km)	R_2 (km)	$(k_2)_1$	$(k_2)_2$	λ_1	λ_2	Λ_1	Λ_2	$\tilde{\Lambda}$	$\delta\tilde{\Lambda}$	$\mathcal{M}_c(M_\odot)$	$\mathcal{R}_c(km)$
NL3	1.20	1.20	14.702	14.702	0.1139	0.1139	7.826	7.826	2983.15	2983.15	2983.15	0.000	1.04	10.350
	1.50	1.20	14.736	14.702	0.0991	0.1139	6.889	7.826	854.06	2983.15	1608.40	220.223	1.17	10.214
	1.25	1.25	14.708	14.708	0.1118	0.1118	7.962	7.962	2388.82	2388.82	2388.82	0.000	1.09	10.313
	1.30	1.30	14.714	14.714	0.1094	0.1094	7.546	7.546	1923.71	1923.71	1923.71	0.000	1.13	10.271
	1.35	1.35	14.720	14.720	0.1070	0.1070	7.393	7.393	1556.84	1556.84	1556.84	0.000	1.18	10.224
	1.35	1.25	14.720	14.708	0.1070	0.1118	7.393	7.962	1556.84	2388.82	1930.02	91.752	1.13	10.268
	1.37	1.25	14.722	14.708	0.1061	0.1118	7.339	7.962	1452.81	2388.82	1863.78	100.532	1.14	10.271
	1.40	1.20	14.726	14.702	0.1044	0.1139	7.231	7.826	1267.07	2983.15	1950.08	183.662	1.13	10.262
	1.40	1.40	14.726	14.726	0.1044	0.1044	7.231	7.231	1267.07	1267.07	1267.07	0.000	1.22	10.174
	1.42	1.29	14.728	14.712	0.1031	0.1099	7.147	7.572	1145.72	1994.02	1515.18	95.968	1.18	10.192
	1.44	1.39	14.730	14.724	0.1027	0.1049	7.120	7.259	1108.00	1311.00	1204.83	19.212	1.23	10.179
	1.45	1.45	14.732	14.732	0.1018	0.1018	7.064	7.064	1037.13	1037.13	1037.13	0.000	1.26	10.124
	1.54	1.26	14.740	14.708	0.0969	0.1114	6.741	7.668	729.95	2303.95	1308.91	168.202	1.21	10.179
	1.60	1.60	14.746	14.746	0.0937	0.0937	6.532	6.532	589.92	589.92	589.92	0.000	1.39	9.979
FSUGarnet	1.20	1.20	12.944	12.944	0.1090	0.1090	3.961	3.961	1469.32	1469.32	1469.32	0.000	1.04	8.983
	1.50	1.20	12.972	12.944	0.0893	0.1090	3.282	3.961	408.91	1469.32	784.09	111.643	1.17	8.847
	1.25	1.25	12.958	12.958	0.1062	0.1062	3.880	3.880	1193.78	1193.78	1193.78	0.000	1.09	8.977
	1.30	1.30	12.968	12.968	0.1030	0.1030	3.777	3.777	945.29	945.29	945.29	0.000	1.13	8.910
	1.35	1.35	12.974	12.974	0.0998	0.0998	3.666	3.666	761.13	761.13	761.13	0.000	1.18	8.860
	1.35	1.25	12.974	12.958	0.0998	0.1062	3.666	3.880	761.13	1193.78	955.00	49.744	1.13	8.920
	1.37	1.25	12.976	12.958	0.0986	0.1062	3.629	3.880	710.62	1193.78	922.54	53.853	1.14	8.924
	1.40	1.20	12.978	12.944	0.0965	0.1090	3.552	3.961	622.06	1469.32	959.22	90.970	1.13	8.904
	1.40	1.40	12.978	12.978	0.0965	0.0965	3.552	3.552	622.06	622.06	622.06	0.000	1.22	8.825
	1.42	1.29	12.978	12.966	0.0949	0.1038	3.495	3.803	565.47	1001.18	755.10	50.492	1.18	8.867
	1.44	1.39	12.978	12.978	0.0939	0.0973	3.456	3.582	531.54	653.60	589.65	14.148	1.23	8.823
	1.45	1.45	12.978	12.978	0.0931	0.0931	3.427	3.427	507.70	507.70	507.70	0.000	1.26	8.776
	1.54	1.26	12.964	12.960	0.0862	0.1057	3.157	3.864	343.73	1146.73	638.35	88.892	1.21	8.817
	1.60	1.60	12.944	12.944	0.0816	0.0816	2.964	2.964	266.20	266.20	266.20	0.000	1.39	8.511
G3	1.20	1.20	12.466	12.466	0.1034	0.1034	3.114	3.114	1776.65	1776.65	1776.65	0.000	1.04	9.331
	1.50	1.20	112.360	12.466	0.0800	0.1034	2.309	3.114	284.92	1776.65	803.43	191.605	1.17	8.890
	1.25	1.25	12.460	12.460	0.1001	0.1001	3.007	3.007	939.79	939.79	939.79	0.000	1.09	8.557
	1.30	1.30	12.448	12.448	0.0962	0.0962	2.875	2.875	728.07	728.07	728.07	0.000	1.13	8.457
	1.35	1.35	12.434	12.434	0.0925	0.0925	2.750	2.750	582.26	582.26	582.26	0.000	1.18	8.398
	1.35	1.25	12.434	12.460	0.0925	0.1001	2.750	3.007	582.26	939.79	742.29	43.064	1.13	8.482
	1.37	1.25	12.428	12.460	0.0909	0.1001	2.696	3.007	530.66	939.79	709.72	49.144	1.14	8.468
	1.40	1.20	12.416	12.466	0.0859	0.1034	2.613	3.114	461.03	1776.65	976.80	183.274	1.13	8.937
	1.40	1.40	12.416	12.416	0.0859	0.0859	2.613	2.613	461.03	461.03	461.03	0.000	1.22	8.312
	1.42	1.29	12.408	12.450	0.0868	0.0972	2.553	2.905	417.96	772.17	571.87	43.226	1.18	8.387
	1.44	1.39	12.398	12.420	0.0854	0.0894	2.501	2.643	384.42	484.90	432.22	12.671	1.23	8.292
	1.45	1.45	12.932	12.392	0.0846	0.0846	2.472	2.472	367.04	367.04	367.04	0.000	1.26	8.225
	1.54	1.26	12.334	12.458	0.0769	0.0992	2.194	2.976	239.49	883.46	474.83	75.175	1.21	8.311
	1.60	1.60	12.280	12.280	0.0716	0.0716	2.000	2.000	179.63	179.63	179.63	0.000	1.39	7.867
IOPB-I	1.20	1.20	13.222	13.222	0.1081	0.1081	4.369	4.369	1654.23	1654.23	1654.23	0.000	1.04	9.199
	1.50	1.20	13.236	13.222	0.0894	0.1081	3.631	4.369	449.62	1654.23	875.35	128.596	1.17	9.044
	1.25	1.25	13.230	13.230	0.1053	0.1053	4.268	4.268	1310.64	1310.64	1310.64	0.000	1.09	9.146
	1.30	1.30	13.238	13.238	0.1024	0.1024	4.162	4.162	1053.07	1053.07	1053.07	0.000	1.13	9.105
	1.35	1.35	13.240	13.240	0.0995	0.0995	4.050	4.050	857.53	857.53	857.53	0.000	1.18	9.074
	1.35	1.25	13.240	13.230	0.0995	0.1053	4.050	4.268	857.53	1310.64	1060.81	49.565	1.13	9.110
	1.37	1.25	13.242	13.230	0.0938	0.1053	4.004	4.268	791.92	1310.64	1019.60	56.371	1.14	9.104
	1.40	1.20	13.242	13.222	0.0960	0.1081	3.911	4.369	680.79	1654.23	1067.64	107.340	1.13	9.097
	1.40	1.40	13.242	13.242	0.0960	0.0960	3.911	3.911	680.79	680.79	680.79	0.000	1.22	8.986
	1.42	1.29	13.242	13.236	0.0949	0.1030	3.864	4.184	632.31	1099.78	835.91	52.836	1.18	9.049
	1.44	1.39	13.242	13.242	0.0935	0.0969	3.806	3.946	578.47	719.80	645.73	17.094	1.23	8.985
	1.45	1.45	13.240	13.240	0.0927	0.0927	3.771	3.771	549.06	549.06	549.06	0.000	1.26	8.915
	1.54	1.26	13.230	13.232	0.0868	0.1047	3.516	4.247	384.65	1253.00	703.58	94.735	1.21	8.991
	1.60	1.60	13.212	12.212	0.0823	0.0823	3.314	3.314	296.81	296.81	296.81	0.000	1.39	8.698

the maximum mass of the NS is $2.15M_\odot$ and the radius (without including crust) of the *canonical* mass is 13.242 km, which is relatively larger as compared to the current x-ray observation radii of range 10.5–12.8 km by Nättilä *et al.* [103] and 11–12 km by Steiner *et al.* [104]. Similarly, FSUGarnet fails to qualify radius constraint. However, recently Annala *et al.* suggested that the radius of a $1.4M_\odot$ star should be in the range $11.1 \leqslant R_{1.4M_\odot} \leqslant 13.4$ km [110], which is consistent with the IOPB-I and FSUGarnet sets. Furthermore, the G3 EoS is relatively softer at energy density $\mathcal{E} \gtrsim 200$ MeV fm^{-3} (see in Fig. 6), which is able to reproduce the recent observational maximum mass of $2.0M_\odot$ as well as the radius of the canonical neutron star mass of 12.416 km.

Now we move to results for the tidal deformability of the single neutron star as well as binary neutron stars (BNSs), which was recently discussed for GW170817 [27]. Equation (41) indicates that λ strongly depends on the radius of the NS as well as on the value of k_2. Moreover, k_2 depends on the internal structure of the constituent body and directly enters into the gravitational wave phase of in-spiraling BNSs, which in turn conveys information about the EoS. As the radii of the NS increases, the deformation by the external field becomes large as there will be an increase in gravitational gradient with the simultaneous increase in radius. In other words, stiff (soft) EoS yields large (small) deformation in the BNS system. Figure 8 shows the tidal deformability as a function of NS mass. In particular, λ takes a wide range of values $\lambda \sim (1\text{–}8) \times 10^{36}$ g cm^2 s^2 as shown in Fig. 8. For the G3 parameter set, the tidal deformability λ is very low in the mass region $0.5M_\odot$–$2.0M_\odot$ in comparison with other sets. This is because the star exerts high central pressure and energy density, resulting in the formation of a compact star which is shown as solid dots in Fig. 6. However, for the NL3 EoS case, it turns out that, because of the stiffness of the EoS, the λ value is increasing. The tidal deformabilities of the canonical NS ($1.4M_\odot$) of IOPB-I along with FSUGarnet and G3 EoSs are found to be 3.191×10^{36}, 3.552×10^{36}, and 2.613×10^{36} g cm^2 s^2, respectively, as shown in Table IV, which are consistent with the results obtained by Steiner *et al.* [111].

Next, we discuss the weighted dimensionless tidal deformability of the BNS of mass m_1 and m_2 which is defined as [27,112,113]

$$\tilde{\Lambda} = \frac{8}{13}[(1+7\eta-31\eta^2)(\Lambda_1+\Lambda_2) + \sqrt{1-4\eta} \times (1+9\eta-11\eta^2)(\Lambda_1-\Lambda_2)], \tag{49}$$

with tidal correction

$$\delta\tilde{\Lambda} = \frac{1}{2}\left[\sqrt{1-4\eta}\left(1-\frac{13272}{1319}\eta+\frac{8944}{1319}\eta^2\right)(\Lambda_1+\Lambda_2) + \left(1-\frac{15910}{1319}\eta+\frac{32850}{1319}\eta^2+\frac{3380}{1319}\eta^3\right)(\Lambda_1-\Lambda_2)\right]. \tag{50}$$

Here, $\eta = m_1m_2/M^2$ is the symmetric mass ratio, m_1 and m_2 are the binary masses, $M = m_1 + m_2$ is the total mass, and Λ_1 and Λ_2 are the dimensionless tidal deformabilities of the BNS, for the case $m_1 \geqslant m_2$. Also, we have taken equal and unequal masses (m_1 and m_2) for the BNS system as has been done in Refs. [114,115]. The calculated results for the Λ_1, Λ_2, and weighted tidal deformability $\tilde{\Lambda}$ of the present EoS are displayed in Table IV. In Fig. 9, we display the different dimensionless tidal deformabilities corresponding to progenitor masses of the NS. It can be seen that the IOPB-I set along with FSUGarnet and G3 sets are in good agreement with the 90% and 50% probability contour of GW170817 [27]. Recently, aLIGO and VIRGO detectors measured a value of $\tilde{\Lambda}$ whose results are more precise than the results found by considering the individual values of Λ_1 and Λ_2 of the BNS [27]. It is noticed that the values of $\tilde{\Lambda} \leqslant 800$ in the low-spin case and $\tilde{\Lambda} \leqslant 700$ in the high-spin case are within the 90% credible intervals which are consistent with the 680.79, 622.06, and 461.03 of the $1.4M_\odot$ NS binary for the IOPB-I, FSUGarnet, and G3 parameter sets, respectively (see Table IV). We also find a reasonably good agreement in the $\tilde{\Lambda}$ value equal to 582.26 for $1.35M_\odot$ in the G3 EoS, which is obtained using a Markov chain Monte Carlo simulation of a BNS with $\tilde{\Lambda} \approx 600$ at a signal-to-noise ratio of 30 in a single aLIGO detector [112,113]. Finally, we close this section with the discussion on chirp mass $\mathcal{M}_c$ and chirp radius $\mathcal{R}_c$ of the BNS system, which are defined as

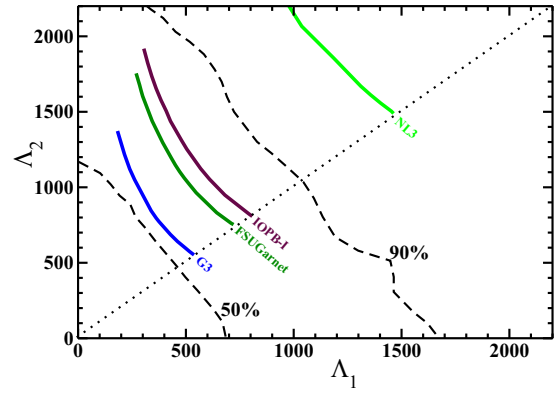

FIG. 9. Different values of Λ generated by using IOPB-I along with NL3, FSUGarnet, and G3 EoS are compared with the 90% and 50% probability contour in the case of low spin, $|\chi| \leqslant 0.05$, as given in Fig. 5 of GW170817 [27].

$$\mathcal{M}_c = (m_1m_2)^{3/5}(m_1+m_2)^{-1/5}, \tag{51}$$

$$\mathcal{R}_c = 2\mathcal{M}_c\,\tilde{\Lambda}^{1/5}. \tag{52}$$

The precise mass measurements of the NSs were reported in Refs. [107,108]. However, until now no observation has been confirmed regarding the radius of the most massive NS. Recently, aLIGO and VIRGO measured a chirp mass of $1.188^{+0.004}_{-0.002}M_\odot$ with very good precision. With the help of this, we can easily calculate the chirp radius $\mathcal{R}_c$ of the BNS system and we find that the chirp radius is in the range $7.867 \leqslant \mathcal{R}_c \leqslant 10.350$ km for equal and unequal-mass BNS systems as shown in Table IV.

V. SUMMARY AND CONCLUSIONS

We have built a new relativistic effective interaction for finite nuclei, infinite nuclear matter, and neutron stars. The

optimization was done using experimental data for eight spherical nuclei such as binding energy and charge radius. The prediction of observables such as binding energies and radii with the new IOPB-I set for finite nuclei is quite good. The $Z = 120$ isotopic chain shows that the magicity appears at neutron numbers $N = 172, 184$, and 198. Furthermore, we find that the IOPB-I set yields slightly larger values for the neutron-skin thickness. This is due to the small strength of the ω-ρ cross-coupling. For infinite nuclear matter at subsaturation and suprasaturation densities, the results of our calculations agree well with the known experimental data. The nuclear matter properties obtained by this new parameter set are nuclear incompressibility $K = 222.65$ MeV, symmetry energy coefficient $J = 33.30$ MeV, symmetry energy slope $L = 63.6$ MeV, and the asymmetry term of nuclear incompressibility, $K_\tau = 389.46$ MeV, at saturation density $\rho_0 = 0.149\,\text{fm}^{-3}$. In general, all these values are consistent with current empirical data. The IOPB-I model satisfies the density dependence of the symmetry energy which is obtained from the different sets of experimental data. It also yields the NS maximum mass to be $2.15 M_\odot$, which is consistent with the current GW170817 observational constraint [109]. The radius of the canonical neutron star is 13.24 km, compatible with the theoretical results in Ref. [110]. Similarly, the predicted values of dimensionless tidal deformabilities are in accordance with the GW170817 observational probability contour [27].

ACKNOWLEDGMENTS

B.K. would like to take this opportunity to convey special thanks to P. Landry and Joonas Nättilä for fruitful discussions and useful suggestions. Furthermore, B.K. is thankful to Swagatika Bhoi for careful reading of the manuscript.

[1] R. J. Furnstahl, B. D. Serot, and H. B. Tang, Nucl. Phys. A **598**, 539 (1996); **615**, 441 (1997).
[2] P. Arumugam, B. K. Sharma, P. K. Sahu, S. K. Patra, Tapas Sil, M. Centelles, and X. Viñas, Phys. Lett. B **601**, 51 (2004).
[3] M. Del Estal, M. Centelles, X. Viñas, and S. K. Patra, Phys. Rev. C **63**, 024314 (2001).
[4] E. Chabanat, P. Bonche, P. Haensel, J. Meyer, and R. Schaeffer, Nucl. Phys. A **635**, 231 (1998).
[5] N. Sandulescu, Nguyen Van Giai, and R. J. Liotta, Phys. Rev. C **61**, 061301(R) (2000).
[6] J. Dobaczewski, H. Flocard, and J. Treiner, Nucl. Phys. A **422**, 103 (1984).
[7] J. Dobaczewski, W. Nazarewicz, T. R. Werner, J. F. Berger, C. R. Chinn, and J. Dechargé, Phys. Rev. C **53**, 2809 (1996).
[8] J. Dechargé and D. Gogny, Phys. Rev. C **21**, 1568 (1980).
[9] J. D. Walecka, Ann. Phys. (N.Y.) **83**, 491 (1974).
[10] J. Boguta and A. R. Bodmer, Nucl. Phys. A **292**, 413 (1977).
[11] P.-G. Reinhard, Rep. Prog. Phys. **52**, 439 (1989).
[12] M. M. Sharma, G. A. Lalazissis, and P. Ring, Phys. Lett. B **317**, 9 (1993).
[13] G. A. Lalazissis, J. König, and P. Ring, Phys. Rev. C **55**, 540 (1997).
[14] G. A. Lalazissis, S. Karatzikos, R. Fossion, D. Pena Arteaga, A. V. Afanasjev, and P. Ring, Phys. Lett. B **671**, 36 (2009).
[15] A. R. Bodmer, Nucl. Phys. A **526**, 703 (1991)
[16] S. Gmuca, Nucl. Phys. A **547**, 447 (1992); J. K. Bunta and S. Gmuca, Phys. Rev. C **68**, 054318 (2003).
[17] Y. Sugahara and H. Toki, Nucl. Phys. A **579**, 557 (1994).
[18] D. Vretenar, G. A. Lalazissis, and P. Ring, Phy. Rev. C **62**, 045502 (2000).
[19] B. G. Todd-Rutel and J. Piekarewicz, Phys. Rev. Lett **95**, 122501 (2005); C. J. Horowitz and J. Piekarewicz, *ibid.* **86**, 5647 (2001); Phys. Rev. C **64**, 062802(R) (2001).
[20] S. Kubis and M. Kutschera, Phys. Lett. B **399**, 191 (1997).
[21] Bharat Kumar, S. K. Singh, B. K. Agrawal, and S. K. Patra, Nucl. Phys. A **966**, 197 (2017).
[22] G. Ferini, M. Colonna, T. Gaitanos, and M. Di Toro, Nucl. Phys. A **762**, 147 (2005).
[23] H. Chiu and E. E. Salpeter, Phys. Rev. Lett. **12**, 413 (1964).
[24] J. N. Bahcall and R. A. Wolf, Phys. Rev. Lett. **14**, 343 (1965).
[25] J. M. Lattimer, C. J. Pethick, M. Prakash, and P. Haensel, Phys. Rev. Lett. **66**, 2701 (1991).
[26] C. J. Horowitz, S. J. Pollock, P. A. Souder, and R. Michaels, Phys. Rev. C **63**, 025501 (2001).
[27] P. B. Abbott *et al.*, Phys. Rev. Lett. **119**, 161101 (2017).
[28] É. É. Flanagan and T. Hinderer, Phys. Rev. D **77**, 021502 (2008).
[29] T. Hinderer, Astrophys. J. **677**, 1216 (2008); **697**, 964(E) (2009).
[30] T. Hinderer, B. D. Lackey, R. N. Lang, and J. S. Read, Phys. Rev. D **81**, 123016 (2010).
[31] J. M. Lattimer and M. Prakash, Phys. Rep. **442**, 109 (2007).
[32] Bharat Kumar, S. K. Biswal, and S. K. Patra, Phys. Rev. C **95**, 015801 (2017).
[33] B. K. Agrawal, S. Shlomo, and V. K. Au, Phys. Rev. C **72**, 014310 (2005).
[34] B. K. Agrawal, Shashi K. Dhiman, and R. Kumar, Phys. Rev. C **73**, 034319 (2006).
[35] Raj Kumar, B. K. Agrawal, and Shashi K. Dhiman, Phys. Rev. C **74**, 034323 (2006).
[36] H. Müller and B. D. Serot, Nucl. Phys. A **606**, 508 (1996).
[37] B. D. Serot and J. D. Walecka, Int. J. Mod. Phys. E **6**, 515 (1997).
[38] S. K. Singh, S. K. Biswal, M. Bhuyan, and S. K. Patra, Phys. Rev. C **89**, 044001 (2014).
[39] R. J. Furnstahl, C. E. Price, and G. E. Walker, Phys. Rev. C **36**, 2590 (1987).
[40] J. P. Elliott and T. H. R. Skyrme, Proc. Soc. London A **232**, 561 (1955).
[41] J. W. Negele, Phys. Rev. C **1**, 1260 (1970).
[42] J. M. Eisenberg and W. Greiner, *Microscopic Theory of the Nucleus* (North-Holland, Amsterdam, 1972).
[43] P. Ring and P. Schuck, *The Nuclear Many-Body Problem* (Springer-Verlag, Berlin, 1980).
[44] Y. K. Gambhir, P. Ring, and A. Thimet, Ann. Phys. (N.Y.) **198**, 132 (1990).
[45] P.-G. Reinhard, M. Rufa, J. Maruhn, W. Greiner, and J. Friedrich, Z. Phys. A **323**, 13 (1986).
[46] B. D. Serot and J. D. Walecka, Adv. Nucl. Phys. **16**, 1 (1986).
[47] W. Kohn and L. J. Sham, Phys. Rev. **140**, A1133 (1965); C. Speicher, R. M. Dreizler, and E. Engel, Ann. Phys. (N.Y.) **213**, 312 (1992).

[48] T. Matsui, Nucl. Phys. A **370**, 365 (1981).
[49] X. Roca-Maza, X. Viñas, M. Centelles, P. Ring, and P. Schuck, Phys. Rev. C **84**, 054309 (2011).
[50] S. K. Singh, M. Bhuyan, P. K. Panda, and S. K. Patra, J. Phys. G: Nucl. Part. Phys. **40**, 085104 (2013).
[51] L.-W. Chen, B.-J. Cai, C.-M. Ko, B.-A. Li, C. Shen, and J. Xu, Phys. Rev. C **80**, 014322 (2009).
[52] M. B. Tsang, J. R. Stone, F. Camera, P. Danielewicz, S. Gandolfi, K. Hebeler, C. J. Horowitz, J. Lee, W. G. Lynch, Z. Kohley, R. Lemmon, P. Möller, T. Murakami, S. Riordan, X. Roca-Maza, F. Sammarruca, A. W. Steiner, I. Vidaña, and S. J. Yennello, Phys. Rev. C **86**, 015803 (2012).
[53] M. Dutra, O. Lourenço, J. S. Sá Martins, A. Delfino, J. R. Stone, and P. D. Stevenson, Phys. Rev. C **85**, 035201 (2012).
[54] C. Xu, B.-A. Li, and L.-W. Chen, Phys. Rev. C **82**, 054607 (2010).
[55] W. G. Newton, M. Gearheart, and B.-A. Li, Astrophys. J. Suppl. Ser. **204**, 9 (2013).
[56] A. W. Steiner and S. Gandolfi, Phys. Rev. Lett. **108**, 081102 (2012).
[57] F. J. Fattoyev, W. G. Newton, J. Xu, and B.-A. Li, Phys. Rev. C **86**, 025804 (2012).
[58] M. Centelles, X. Roca-Maza, X. Viñas, and M. Warda, Phys. Rev. Lett. **102**, 122502 (2009).
[59] B. A. Li and X. Han, Phys. Lett. B **727**, 276 (2013).
[60] S. Kirkpatrick, C. D. Gelatt, and M. P. Vecchi, Science **220**, 671 (1983).
[61] W. H. Press, S. A. Teukolsky, W. T. Vetterling, and B. P. Flannery, *Numerical Recipes in Fortran* (Cambridge University Press, New York, 1992).
[62] S. Kirkpatrick, J. Stat. Phys. **34**, 975 (1984).
[63] L. Ingber, Math. Comput. Model. **12**, 967 (1989).
[64] B. Cohen, Master's thesis, Tel-Aviv University, 1994 (unpublished).
[65] J. Dobaczewski, W. Nazarewicz, and P.-G. Reinhard, J. Phys. G: Nucl. Part. Phys. **41**, 074001 (2014).
[66] P. Klüpfel, P.-G. Reinhard, T. J. Bürvenich, and J. A. Maruhn, Phys. Rev. C **79**, 034310 (2009).
[67] W.-C. Chen and J. Piekarewicz, Phys. Lett. B **748**, 284 (2015).
[68] M. Wang, G. Audi, A. H. Wapstra, F. G. Kondev, M. MacCormick, X. Xu, and B. Pfeiffer, Chin. Phys. C **36**, 1603 (2012).
[69] I. Angeli and K. P. Marinova, At. Data Nucl. Data Tables **99**, 69 (2013).
[70] S. K. Patra, Int. J. Mod. Phys. E **2**, 471 (1993).
[71] R. F. Garcia Ruiz *et al.*, Nat. Phys. **12**, 594 (2016).
[72] P.-G. Reinhard and W. Nazarewicz, Phys. Rev. C **81**, 051303(R) (2010).
[73] X. Roca-Maza, M. Centelles, X. Viñas, and M. Warda, Phys. Rev. Lett. **106**, 252501 (2011).
[74] B. A. Brown, Phys. Rev. Lett. **85**, 5296 (2000).
[75] S. Abrahamyan *et al.*, Phys. Rev. Lett. **108**, 112502 (2012).
[76] A. Trzcińska, J. Jastrzebski, P. Lubiński, F. J. Hartmann, R. Schmidt, T. von Egidy, and B. Klos, Phys. Rev. Lett. **87**, 082501 (2001); J. Jastrzebski, A. Trzcińska, P. Lubiński, B. Klos, F. J. Hartmann, T. von Egidy, and S. Wycech, Int. J. Mod. Phys. E **13**, 343 (2004).
[77] X. Viñas, M. Centelles, X. Roca-Maza, and M. Warda, Eur. Phys. J. A **50**, 27 (2014).
[78] F. J. Fattoyev, J. Piekarewicz, and C. J. Horowitz, arXiv:1711.06615.
[79] J. Zenihiro, H. Sakaguchi, T. Murakami, M. Yosoi, Y. Yasuda, S. Terashima, Y. Iwao, H. Takeda, M. Itoh, H. P. Yoshida, and M. Uchida, Phys. Rev. C **82**, 044611 (2010).
[80] P. Möller, A. J. Sierk, T. Ichikawa, and H. Sagawa, At. Data Nucl. Data Tables **109**, 1 (2016).
[81] K. Rutz, M. Bender, T. Bürvenich, T. Schilling, P.-G. Reinhard, J. A. Maruhn, and W. Greiner, Phys. Rev. C **56**, 238 (1997).
[82] R. K. Gupta, S. K. Patra, and W. Greiner, Mod. Phys. Lett. A **12**, 1727 (1997).
[83] S. K. Patra, C.-L. Wu, C. R. Praharaj, and R. K. Gupta, Nucl. Phys. A **651**, 117 (1999).
[84] M. S. Mehta, Harvinder Kaur, Bharat Kumar, and S. K. Patra, Phys. Rev. C **92**, 054305 (2015).
[85] M. Bhuyan and S. K. Patra, Mod. Phys. Lett. A **27**, 1250173 (2012).
[86] G. Coló, U. Garg, and H. Sagawa, Eur. Phys. J. A **50**, 26 (2014).
[87] J. Piekarewicz, Eur. Phys. J. A **50**, 25 (2014).
[88] J. R. Stone, N. J. Stone, and S. A. Moszkowski, Phys. Rev. C **89**, 044316 (2014).
[89] J. M. Pearson, N. Chamel, and S. Goriely, Phys. Rev. C **82**, 037301 (2010).
[90] T. Li, U. Garg, Y. Liu, R. Marks, B. K. Nayak, P. V. Madhusudhana Rao, M. Fujiwara, H. Hashimoto, K. Nakanishi, S. Okumura, M. Yosoi, M. Ichikawa, M. Itoh, R. Matsuo, T. Terazono, M. Uchida, Y. Iwao, T. Kawabata, T. Murakami, H. Sakaguchi, S. Terashima, Y. Yasuda, J. Zenihiro, H. Akimune, K. Kawase, and M. N. Harakeh, Phys. Rev. C **81**, 034309 (2010).
[91] U. Garg *et al.*, Nucl. Phys. A **788**, 36 (2007).
[92] P. Danielewicz and J. Lee, Nucl. Phys. A **922**, 1 (2014).
[93] M. B. Tsang, Y. Zhang, P. Danielewicz, M. Famiano, Z. Li, W. G. Lynch, and A. W. Steiner, Phys. Rev. Lett. **102**, 122701 (2009); Int. J. Mod. Phys. E **19**, 1631 (2010).
[94] P. Russotto *et al.*, Phys. Rev. C **94**, 034608 (2016).
[95] M. Baldo and C. Maieron, Phys. Rev. C **77**, 015801 (2008).
[96] B. Friedman and V. R. Pandharipande, Nucl. Phys. A **361**, 502 (1981).
[97] S. Gandolfi, A. Yu. Illarionov, S. Fantoni, F. Pederiva, and K. E. Schmidt, Phys. Rev. Lett. **101**, 132501 (2008).
[98] A. Gezerlis and J. Carlson, Phys. Rev. C **81**, 025803 (2010).
[99] K. Hebeler, J. M. Lattimer, C. J. Pethick, and A. Schwenk, Astrophys. J. **773**, 11 (2013).
[100] C. Mondal, B. K. Agrawal, J. N. De, and S. K. Samaddar, Phys. Rev. C **93**, 044328 (2016).
[101] P. Danielewicz, R. Lacey, and W. G. Lynch, Science **298**, 1592 (2002).
[102] M. Prakash, T. L. Ainsworth, and J. M. Lattimer, Phys. Rev. Lett. **61**, 2518 (1988).
[103] J. Nättilä, A. W. Steiner, J. J. E. Kajava, V. F. Suleimanov, and J. Poutanen, Astron. Astrophys. **591**, A25 (2016).
[104] A. W. Steiner, J. M. Lattimer, and E. F. Brown, Astrophys. J. **722**, 33 (2010).
[105] P. Landry and E. Poisson, Phys. Rev. D **89**, 124011 (2014).
[106] J. R. Oppenheimer and G. M. Volkoff, Phys. Rev. **55**, 374 (1939); R. C. Tolman, *ibid.* **55**, 364 (1939).

[107] P. B. Demorest, T. Pennucci, S. M. Ransom, M. S. E. Roberts, and J. W. T. Hessels, Nature (London) **467**, 1081 (2010).
[108] J. Antoniadis *et al.*, Science **340**, 1233232 (2013).
[109] L. Rezzolla, Elias R. Most, and Lukas R. Weth, Astrophys. J. Lett. **852**, L25 (2018).
[110] E. Annala, Tyler Gorda, Aleksi Kurkela, and Aleksi Vuorinen, arXiv:1711.02644.
[111] A. W. Steiner, S. Gandolfi, F. J. Fattoyev, and W. G. Newton, Phys. Rev. C **91**, 015804 (2015).
[112] M. Favata, Phys. Rev. Lett. **112**, 101101 (2014).
[113] L. Wade, J. D. E. Creighton, E. Ochsner, B. D. Lackey, B. F. Farr, T. B. Littenberg, and V. Raymond, Phys. Rev. D **89**, 103012 (2014).
[114] P. B. Abbott *et al.*, Astrophys. J. Lett. **851**, L16 (2017).
[115] D. Radice, A. Perego, and F. Zappa, Astrophys. J. Lett. **852**, L29 (2018).
[116] F. Ozel, G. Baym, and T. Guver, Phys. Rev. D **82**, 101301 (2010).
[117] V. Suleimanov, J. Poutanen, M. Revnivtsev, and K. Werner, Astrophys. J. **742**, 122 (2011).